Chapter 4

EFFECT OF Mn DOPING ON THE ELECTRONIC AND OPTICAL PROPERTIES OF $Dy_2Ti_2O_7$: A COMBINED SPECTROSCOPIC AND THEORETICAL STUDY

4.1 Introduction

After studying the spin dynamics of the Mn-doped derivative of $Dy_2Ti_2O_7$, we tried to look for its applications in relevance to devices and explored its optical and electronic properties. $Dy_2Ti_2O_7$, being a multiferroic system, possesses interesting fundamentals and offers the possibility of application of such systems in various spintronic devices [104]–[106]. Besides exhibiting rich exotic magnetic properties, such systems could be exploited for studying their optical properties [107]–[109]. Several of the unusual spectroscopic properties of these pyrochlore oxides are associated with the large crystalline field that splits the electronic states of the $4f^n$ configuration of the rare earth ions [110]. A comparative study of the crystal electric field, acting on the 4f electron site based on lattice-sum calculations, was developed by Morrison [111], [112]. The inter-configurational mixing of electronic states results in different magnitudes and distributions of transition intensities within the $4f^n$ electronic configuration through the substitution of non-magnetic atoms at rare earth site or by varying the rare earth ion (Pr^{3+}, Eu^{3+}, Yb^{3+}, etc.) itself [113]. Transition metal oxides are of particular interest, partly due to complexities associated with d-shell electrons [114]. The 3d elements form a number of oxygen-containing clusters and compounds with variable oxidation states of the metal

cation. Previous studies suggest that because of the remarkable optical properties of Mn^{4+}, its inclusion in a variety of lattice structures offers practical applications, like luminescence in solids, potential materials for holographic recording, optical data storage, the laser application and in thermoluminescence dosimetry, etc. [115]–[120].

This chapter aims to establish a correlation between the structural and optical properties of these pyrochlore oxides. Computational approach and spectroscopic techniques have been applied to study the electronic structure of the valence Band (V.B.) and conduction Band (C.B.), band gap energy (E_g), orbitals involved in hybridization, influence of the crystal structure, and effect of perturbation on the electronic and optical properties. In the first section, we will discuss the electronic structure studies of $Dy_2Ti_{2-x}Mn_xO_7$ (x = 0, 0.05, 0.10, 0.15, 0.20) series. We start with the calculation of band structure and density of states using density functional theory (DFT) calculations. The effect of Mn inclusion on phonon behavior in the $Dy_2Ti_2O_7$ matrix was studied using Raman spectroscopy. Another powerful tool for the characterization of local electronic structure and electronic correlation effects is the XPS. This technique is based on the excitation of electrons from deeply bound core levels to unoccupied levels. Section 2 deals with our essential findings that reveal the crystal field states identified through the optical measurement techniques, namely UV-visible absorption photoluminescence (PL) emission spectroscopy.

4.1.1 Theoretical calculation of electronic structure using density functional theory (DFT) calculations.

In $Dy_2Ti_2O_7$ pyrochlore structures, corner-sharing TiO_6 octahedra are the basic building units. Dy-site cations are relatively electropositive ions, and the Dy_2O2 chains do not interact strongly with each other even though they form an interpenetrating network. Thus, the energy band-gap depends on the corner-sharing octahedral network TiO_6 instead of Dy-site cations. The substantial reduction and enhancement in Ti-O bond length (from 1.944(2) Å to 1.936(2) Å) and O-Ti-O bond angle (from 85.21(2) ° to 85.73(2) °) is related to the octahedral distortion **(Table 4.1)**. The Dy coordinates parameter does not evolve much, as given in **Table 4.1.**

Table 4.1 Structural parameters including lattice parameters, bond length and bond angle obtained from Rietveld refinement of high-resolution x-ray diffraction data of $Dy_2Ti_{2-x}Mn_xO_7$.

Compound	Experimental lattice parameter(Å)	Bond Length (Å)				Bond Angle (°)		
$Dy_2Ti_{2-x}Mn_xO_7$		Dy-O1	Dy-O2	Ti-O	Dy-Dy	O1-Dy-O2	O1-Dy-O1	O1-Ti-O1
x = 0	10.1293(5)	2.5210(3)	2.1931(0)	1.9443(2)	3.5813(0)	80.01(7)	62.95(4)	85.21(2)
x = 0.05	10.1285(6)	2.5250(3)	2.1929(0)	1.9418(2)	3.5809(3)	80.11(7)	62.89(4)	85.44(2)
x = 0.10	10.1268(6)	2.5370(3)	2.1923(0)	1.9347(2)	3.5800(3)	80.38(7)	62.73(4)	86.07(2)
x = 0.15	10.1214(6)	2.5350(3)	2.1913(0)	1.9342(2)	3.5784(3)	80.37(7)	62.74(4)	86.04(2)
x = 0.20	10.1182(4)	2.5280(3)	2.1906(0)	1.9367(2)	3.5773(0)	80.24(7)	62.82(4)	85.73(2)

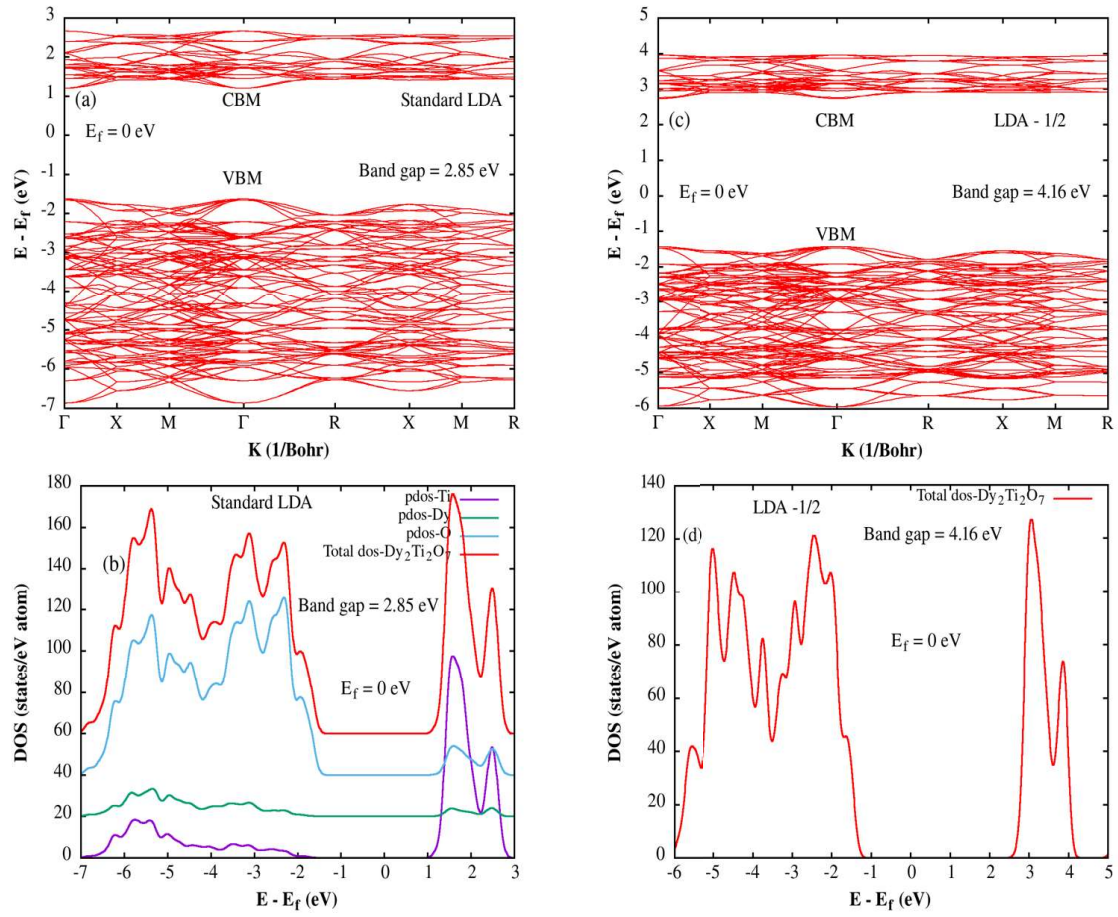

Figure 4.1 Calculated (a) band Structure, and (b) total density of state along with partial density of states for $Dy_2Ti_2O_7$ using LDA. Calculated (c) band Structure and (d) total density of state for $Dy_2Ti_2O_7$ using LDA -1/2.

Calculated total density of states and partial density of states (PDOSs) of $Dy_2Ti_2O_7$ using local density approximation (LDA) is shown in **Figure 4.1 (b)**. PDOSs reveal the significant contribution of the O-2p state hybridized with Dy-5p, Dy-5d and Ti-3d states for forming valence band states. The lower-lying states in the valence band are primarily dominated by O-2p, Ti-3d, Dy-5s and Dy-5d states, along with a bit of contribution from Dy-5p and O-2s states, whereas Dy-5d states and Ti-3d states majorly contribute to conduction band formation. Using LDA, the computed band-gap for $Dy_2Ti_2O_7$ from total density of states

(DOS) is 2.85 eV, as shown in **Figure 4.1 (a).** Using self-energy correction through LDA-1/2, the total DOS is shown in **Figure 4.1 (d)** [121]. An increase in the cross-section near the conduction band edge is most likely to be associated with the O-2p state. Introducing self-energy potential centered at the anion site to cancel the energy associated with electron-hole recombination helps to predict a much more accurate band-gap in such systems. The conduction-band edge shifts away from the Fermi-level, and the obtained band gap is 4.16 eV, which approaches near to the experimentally obtained band gap of 3.82 eV. As shown in **Figure 4.1 (c)**, band structure indicates gamma points as the maxima and minima of the valence and conduction band, respectively, showing direct band-gap transition in $Dy_2Ti_2O_7$ using both LDA and LDA-1/2.

We further investigated the effect of band-gap modulation with Mn inclusion at Ti site in $Dy_2Ti_2O_7$. With five percent (x = 0.10) inclusion of Mn at Ti site, a state emerges at the Fermi level, as could be seen from the total and partial density of states using LDA shown in **Figure 4.2 (b),** and the obtained band gap is 1.45 eV. Hybridized orbitals are consistent with that of $Dy_2Ti_2O_7$ along with the additional involvement of Mn^{4+} 3d state for the formation of C.B. and V.B. Mn-3d and O-2p states majorly appear at a Fermi level, indicating the interaction between these states due to the charge transfer effect between the Mn-3d orbitals (Mn^{3+}) and O-2p ligand orbitals in Mn-based systems associated with spin-flip between the low spin and high spin state.

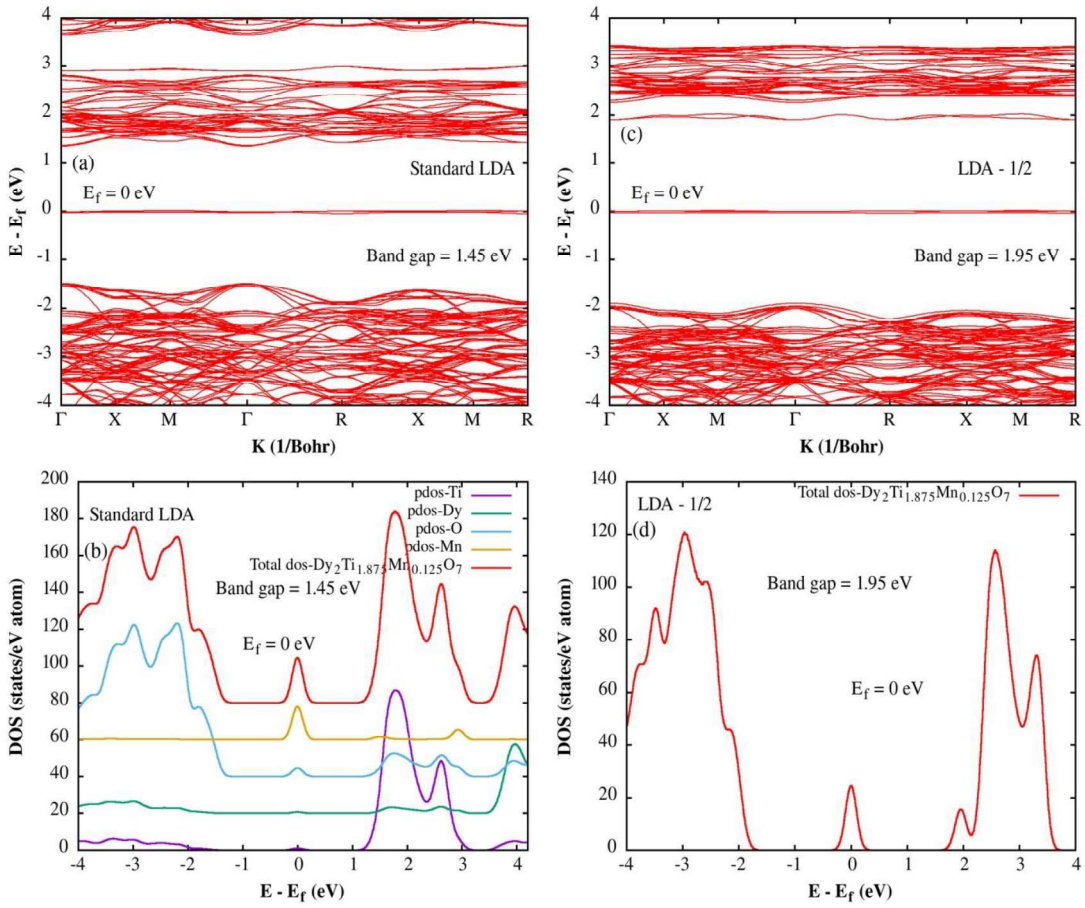

Figure 4.2 Calculated (a) band Structure, and (b) total density of state along with partial density of states for $Dy_2Ti_{1.9}Mn_{0.1}O_7$ using LDA. Calculated (c) band Structure and (d) total density of state for $Dy_2Ti_{1.9}Mn_{0.1}O_7$ using LDA -1/2

Figure 4.2 (a) shows the band structure indicates direct transition involving the gamma high symmetry point. Using LDA-1/2, the total density of state, as shown in **Figure 4.2(d)**, indicates the same orbital contribution for band formation as in LDA. Additionally, a small cross-section appears at the C.B. edge in LDA-1/2, leading to a reduction in band-gap from 4.16 eV (x = 0) to 1.95 eV (x = 0.1) with Mn inclusion. Gamma is the high symmetry point

involved in direct band-gap transition, and the band structure for x = 0.1 is shown in **Figure 4.2 (c).**

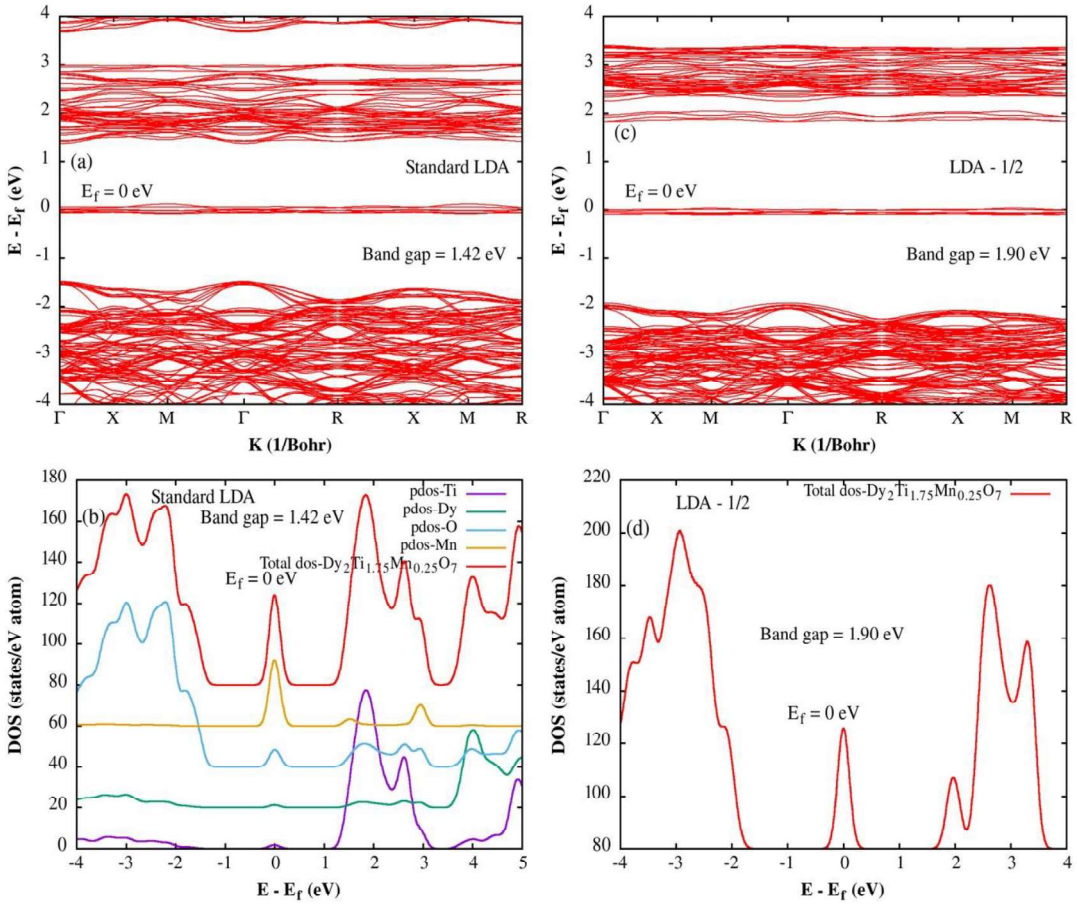

Figure 4.3 Calculated (a) band Structure, and (b) total density of state along with partial density of states for $Dy_2Ti_{1.8}Mn_{0.2}O_7$ using LDA. Calculated (c) band Structure and (d) total density of state for $Dy_2Ti_{1.8}Mn_{0.2}O_7$ using LDA -1/2.

Partial density of states for x = 0.2 using LDA is shown in **Figure 4.3 (b).** An increase in the percentage inclusion of Mn results in the enhancement in the cross-section of its d state and O-2p state at the Fermi level. Along with the contribution of Mn -3d and O-2p state at the Fermi level, Ti-3d and Dy-5d states also participate in hybridization for the formation of V.B.

and C.B. Theoretically obtained band-gap for x = 0.2 is 1.42 eV as obtained from the band structure and total density of state as shown in **Figure 4.3 (a)** and **Figure 4.3 (b)** respectively. LDA-1/2 results in a band gap of 1.90 eV as obtained from the band structure and total density of states as shown in **Figure 4.3 (c)** and **Figure 4.3 (d).** As discussed earlier through the Jahn-Teller effect, the theoretical calculation also indicates the presence of a mixed state of Mn, resulting in the intermediate Mn state between V.B and C.B with immediate inclusion of Mn at Ti site in the $Dy_2Ti_{2-x}Mn_xO_7$ system.

4.1.2 Raman spectroscopy

Room temperature Raman measurement was performed with an excitation wavelength of 532 nm to study the effect of Mn inclusion on phonon behavior in the $Dy_2Ti_2O_7$ matrix. **Figure 4.4** shows the Raman spectra of the $Dy_2Ti_{2-x}Mn_xO_7$ sample in the wave number range of (150 – 850) cm^{-1}. The most prominent Raman mode for the $Dy_2Ti_2O_7$ system is observed at 306 cm^{-1}, corresponding to two modes, namely F_{2g} and E_g, with very close wavenumbers. The next mode is detected at around 515 cm^{-1} and is associated with the A_{1g} mode. The A_{1g} mode observed at 515 cm^{-1} plays a significant role in the pyrochlore structure and is related to the stretching motion of Ti-O bonds and the bending of O-Ti-O angles in the TiO_6 octahedra of $Dy_2Ti_2O_7$ system [122]–[125].

According to Mackza et al., Raman spectra of a pyrochlore structure ($A_2B_2O_7$) should possess six Raman active fundamental modes distributed among $A_{1g} + E_g + 4F_{2g}$ irreducible representations. Since A and B cations of 16d and 16c sites give inactive Raman phonon modes, the mentioned modes involve only the motion of oxygen atoms. Categorically, oxygen atoms located at 48f positions, which are bonded to two A and two B cations, contribute to

five phonon modes ($A_{1g} + E_g + 3F_{2g}$), while oxygen located at 8b site, which is tetrahedrally bonded to only A cations, gives single F_{2g} mode [126]–[129]. With Mn inclusion, F_{2g} mode at 215 cm^{-1} and $F_{2g} + E_g$ mode at 306 cm^{-1} is suppressed, and new F_{2g} mode at 425 cm^{-1} emerges along with the distortion of A_{1g} mode at 518 cm^{-1}. The modulation of the x parameter of the oxygen atom at the 48f site is directly linked to the A_{1g} mode. Mn inclusion sets distortion in the crystal lattice and gives rise to a new F_{2g} mode at 560 cm^{-1}.

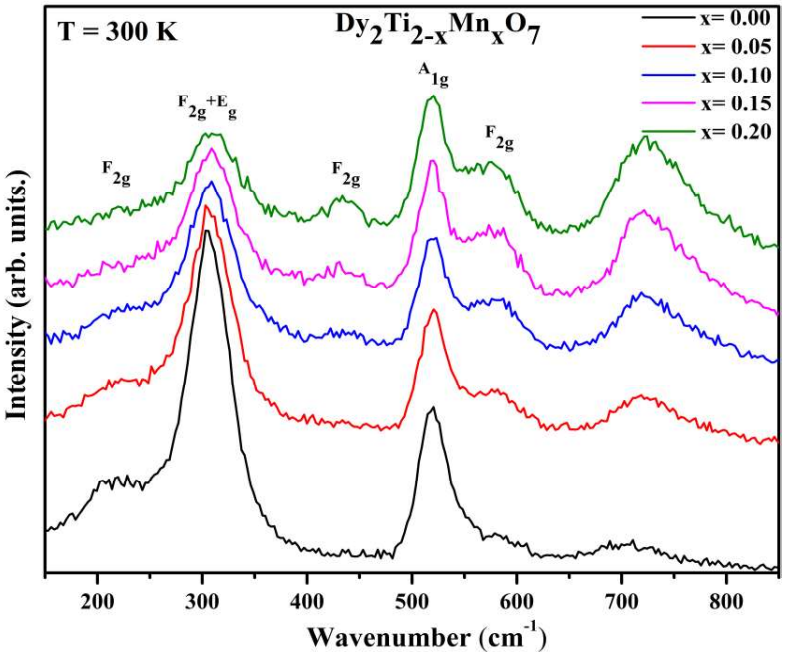

Figure 4.4 Room temperature Raman spectra for $Dy_2Ti_{2-x}Mn_xO_7$ (x = 0, 0.05, 0.10, 0.15, 0.20) showing the presence of Raman modes corresponding to pyrochlore structure.

The mixture of Dy−O and Ti−O, bond stretching vibrations, is related to the F_{2g} mode. Peak intensity at 720 cm^{-1} may be due to the structural change due to presence of Mn ions in the crystal structure, which can interact with the neighboring oxygen atoms and modify the

vibrational modes associated with the A_{1g} and F_{2g} Raman-active modes. The changes in peak intensity can be attributed to changes in the local crystal field and symmetry of the system caused by the Mn substitution. The broadening of the peak at 306 cm^{-1} with increasing Mn concentration indicates significant local disordering, and it suggests a decrease in symmetry due to the Jahn-Teller distortion [130]. Overall, these changes in the Raman spectra suggest distortion of the octahedral structure, and the incorporation of Mn into the lattice upon substitution.

4.1.3 XPS spectroscopy

Core-level electronic interaction in the $Dy_2Ti_{2-x}Mn_xO_7$ system has been studied through x-ray photoelectron spectroscopy (XPS). A survey scan (wide surface) and detailed elemental scan (Dy-3d, Ti-2p and O-1s) for the $Dy_2Ti_2O_7$ system is shown in **Figure 4.5.** The survey scan confirmed that all constituent elements were present in the compound. Further, all peaks in the spectra are assigned their electronic states as per the binding energy obtained from the XPS data book [131]. Except for the presence of C-1s peak at 284 eV in the form of impurity being absorbed from the air, all the identified peaks belong to Dy, Ti and O states for the $Dy_2Ti_2O_7$ system. This surface-absorbed/adsorbed carbon has been found in many systems, but it does not affect any of its physical properties. The survey scan of $Dy_2Ti_2O_7$ presents the KLL Auger oxygen peak at 766 and 780 eV, as shown in **Figure 4.5 (a)**. The Auger feature diminishes gradually with Mn inclusion [**Figure 4.6 (a)**] and finally disappears for x = 0.2 [**Figure 4.7 (a)**].

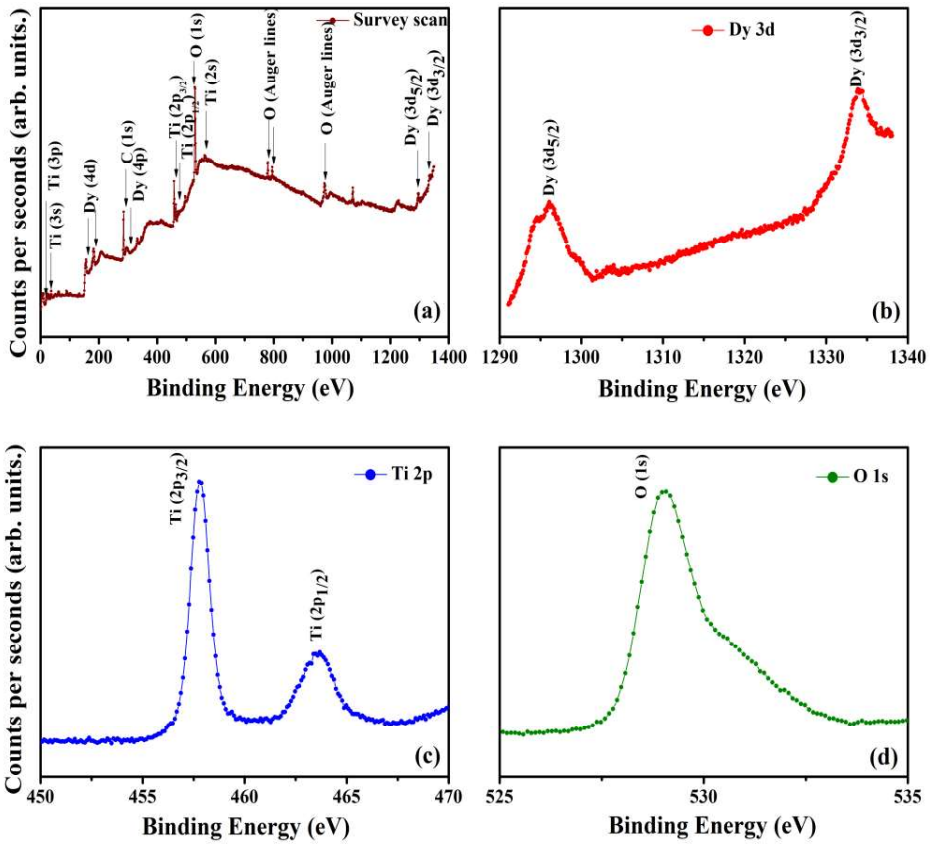

Figure 4.5 X-ray photoelectron spectroscopy (XPS) (a) survey scan for $Dy_2Ti_2O_7$ and core level XPS spectra for its constituent elements (b) Dy-3d, (c) Ti-$2p_{1/2}$, and (d) O-1s states.

Further O-1s spectra at 529 eV in $Dy_2Ti_2O_7$ split into two parts with Mn inclusion (x = 0.1 & 0.2), one at binding energy position 531.3 eV and the other at 529.3 eV. The splitting of the peak at 529.3 eV could be attributed to a change in the local electronic structure around oxygen atoms caused by the presence of Mn ions, resulting in a different hybridization between oxygen and metal atoms. These two peak structures are attributed to lattice oxygen at lower binding energies and to surface or defect-related oxygen at higher binding energies. The peak at 529.3 eV corresponds to the oxygen present at the lattice site denoted by O_L, and

that at 531.3 eV corresponds to the oxygen (O_C) that is chemisorbed from the surface or due to the creation of oxygen vacancies (Ov) [132], [133].

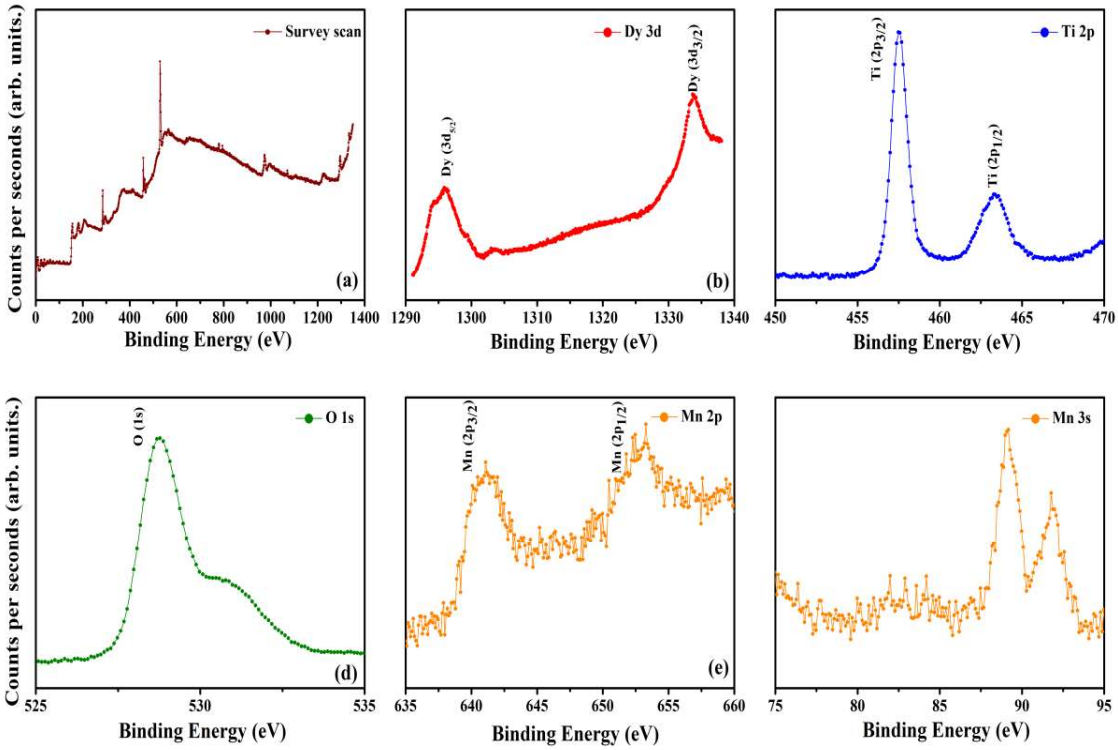

Figure 4.6 x-ray photoelectron spectroscopy (XPS) (a) survey scan for $Dy_2Ti_{1.9}Mn_{0.10}O_7$ and core level XPS spectra for its constituent elements (b) Dy-3d, (c) Ti-2p, (d) O-1s, (e) Mn-2p and (f) Mn-3s states

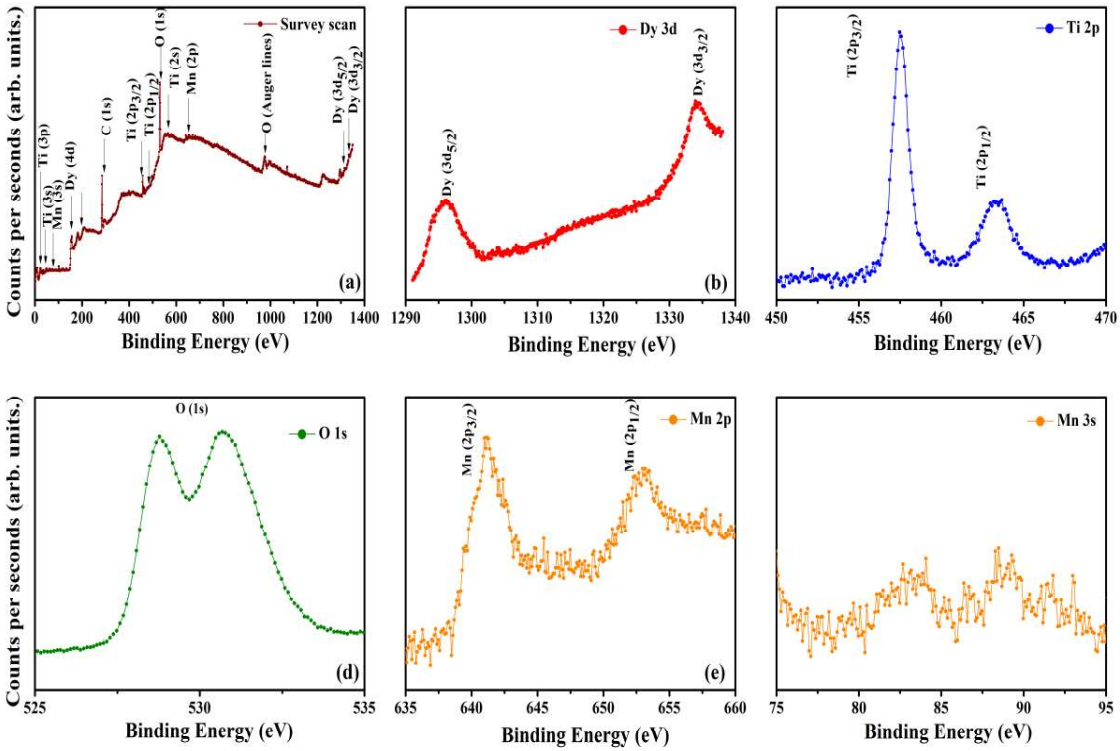

Figure 4.7 x-ray photoelectron spectroscopy (XPS) (a) survey scan for $Dy_2Ti_{1.8}Mn_{0.20}O_7$ and core level XPS spectra for its constituent elements (b) Dy-3d, (c) Ti-2p, (d) O-1s, (e) Mn-2p and (f) Mn-3s states.

Figure 4.8 depicts the peak fitted XPS spectrum of Mn-3s core-level. The two exchange splitting peaks centered around 83.76 eV and 88.46 eV ($\Delta E_{3s} \sim 5.1$ eV). Based on the measured Mn-3s level splitting E3s, the Mn valence v_{Mn} was calculated using a linear equation [134], [135];

$$v_{Mn} = 9.67 - 1.27 \times E_{3s}/eV$$

The Mn valence state obtained from the above relation is 3.2+, supporting the co-existence of the Mn^{+3} state along with Mn^{4+}, thereby creating oxygen vacancy, as mentioned earlier. The

conversion of Mn^{+4} to Mn^{+3} results in the Jahn-Teller effect due to the induced lattice distortion (**Table 4.1)** with the increasing percentage of Mn at the Ti site in $Dy_2Ti_2O_7$. There is a systematic variation in the intensity of binding energy of Mn-$2p_{1/2}$ state at 650 eV and Mn-$2p_{3/2}$ state at 639 eV indicating interaction between Mn-2p and O-1s states. Core level XPS spectra for the Ti^{4+}-2p state present the spin-orbit split peaks at 457 eV and 463 eV for Ti-$2p_{3/2}$ and Ti-$2p_{1/2}$ states, respectively that corroborate well with the earlier reports for tetravalent states of Ti. Detailed Dy^{3+} spectra contain two spin-orbit coupling peaks corresponding to Dy-$3d_{5/2}$ (1296 eV) and Dy-$3d_{3/2}$ (1333 eV) states. Dy-3d state has no subsequent effect with Mn inclusion at Ti site as shown in **Figure 4.6 (b)** and **Figure 4.7 (b).**

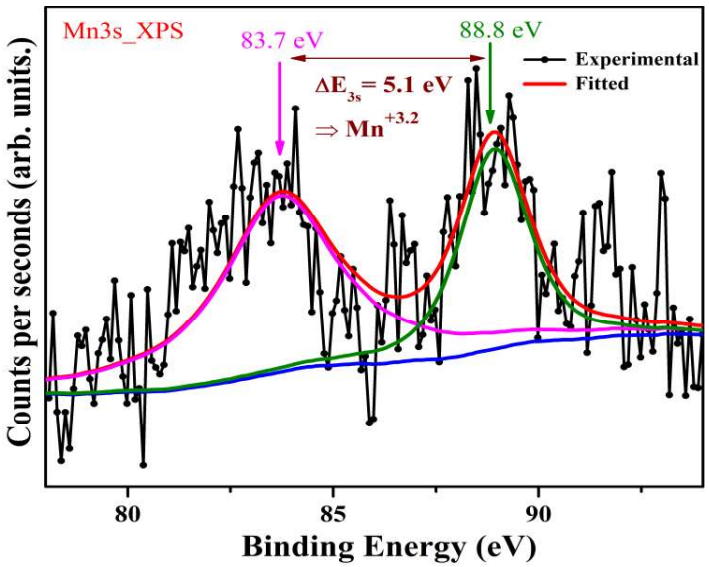

Figure 4.8 x-ray photoelectron spectroscopy (XPS) survey scan for Mn-3s state for $Dy_2Ti_{1.8}Mn_{0.20}O_7$.

4.2 Optical Studies on $Dy_2Ti_{2-x}Mn_xO_7$ System

4.2.1 Ultraviolet-visible spectroscopy

UV-Visible absorption spectra for the $Dy_2Ti_{2-x}Mn_xO_7$ system are recorded in the 200-1400 nm range, as shown in **Figure 4.9**. Ti^{4+} absorption states have been identified at 214 and 300 nm. The peak centred at 214 nm in $Dy_2Ti_2O_7$ corresponds to ligand-to-metal charge transfer (LMCT) from the O-2p orbital of the valence band to Ti-4d of the conduction band [136]. The absorption peak centred at 300 nm in $Dy_2Ti_2O_7$ corresponds to LMCT from the O-2p orbital of the valence band to the Ti-3d orbital of the conduction band. With immediate Mn inclusion at the Ti site, the absorption peak at 300 nm shifts to 340 nm, thereby pushing the Ti-3d state towards the lower energy side in the conduction band (CB). It indicates that Mn-O interaction reduces the energy gap between Ti-3d and O-2p state. It is justified by the systematic increase in the Ti-O1-Ti bond angle from 85.21° (2) for x = 0 to 85.73° (2) for x = 0.20 (**Table 4.1**). The increase in the angular separation with the increase in percentage inclusion of Mn^{4+} reduces the extent of hybridization between the O-2p and Ti-3d state, resulting in the lowering of the Ti-3d energy state. Additionally, in $Dy_2Ti_{2-x}Mn_xO_7$, Mn is present in the +4-oxidation state as it replaces Ti^{4+} at the octahedral site. The octahedral crystal field creates a large energy gap between the occupied t_{2g} and unoccupied e_g orbital of Ti^{4+} [137]. It shifts the e_g state towards lower energy; hence, the Ti^{4+}-3d state is shifted towards a higher wavelength with an increase in x. A new Mn^{4+} absorption state emerges at 455 nm for x = 0.05 in $Dy_2Ti_{2-x}Mn_xO_7$. Transitions corresponding to higher wavelength regions in the absorption spectrum between 700-1400 nm are correlated to charge transfer transition (CTT) as an internal transition within the 4f shells of Dy^{3+} ion [136]. The free ion ground state is

$^6H_{15/2}$, Dy^{3+} being Kramers ion possess all ground state doublet state resulting into sixteen (2S+1; 15/2+1 = 16) electronic states which are 8 doublets ranging from Z_1 to Z_8 [51]. The CTT peaks of Dy^{3+} ion being centred at 738, 789, 873, 1048, 1087 and 1262 nm are identified as absorption from $^6H_{15/2}$ (ground state) to $^6F_{3/2}$, $^8F_{5/2}$, $^8F_{7/2}$, $^6H_{5/2}$, $^6F_{9/2}$ and $^6F_{11/2}$ excited states respectively [113], [138] Further, band-gap (E_g) has been determined by employing the Tauc equation to absorption spectrum; $\alpha h\nu = A\ (h\nu - E_g)$, where A is constant related to materials, ν is the frequency of the incident photon, α is absorption coefficient, E_g is the band transition energy, n decides the type of transition, and it depends upon the material (n = 2 for direct and n = ½ for indirect electronic transition) [139].

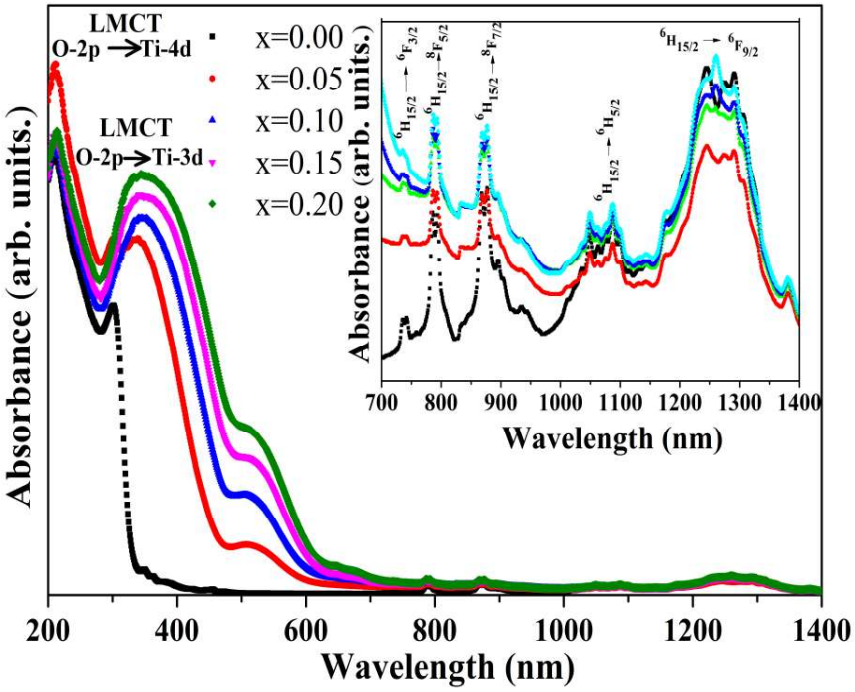

Figure 4.9 Room temperature ultraviolet-visible (UV-vis) absorption spectrum of polycrystalline $Dy_2Ti_{2-x}Mn_xO_7$ (x = 0, x = 0.05, x = 0.10, x = 0.15 and x = 0.20) compound in 200–1400 nm wavelength range. Inset shows the UV–Vis spectrum in 700–1400 nm wavelength range.

The band gap was calculated for the allowed direct transition by noting the intercept value on the photon energy axis extrapolated up to 0 eV in a linear fit of $(\alpha h\nu)^2$ versus hν, as shown in **Figure 4.10.** Using this equation, band-gap (E_g) for $Dy_2Ti_2O_7$ comes out to be 3.82 eV, which is equated to the absorption peak at 300 nm (1240/300 = 4.1 eV) corresponding to electronic transition involving O^{2-}-2p orbital to Ti^{3+}-3d orbital. E_g reduces to 2.84 eV for x = 0.05, and the band-gap for all values of x is shown in **Table 4.2**. Immediate reduction in bandgap to 2.84 eV for x = 0.05 is attributed to the emergence of the Mn state at 455 nm (1240/455 = 2.72 eV) identified as LMCT from O-2p to Mn-3d state. An increase in the percentage inclusion of Mn results in a sequential reduction in band-gap from 2.84 to 2.45 eV. This is attributed to the reduction in lattice parameter with the increase in Mn concentration. Ti/Mn-O separation reduces from 1.9443(2) Å for x = 0 to 1.9367(2) Å for x = 0.2.

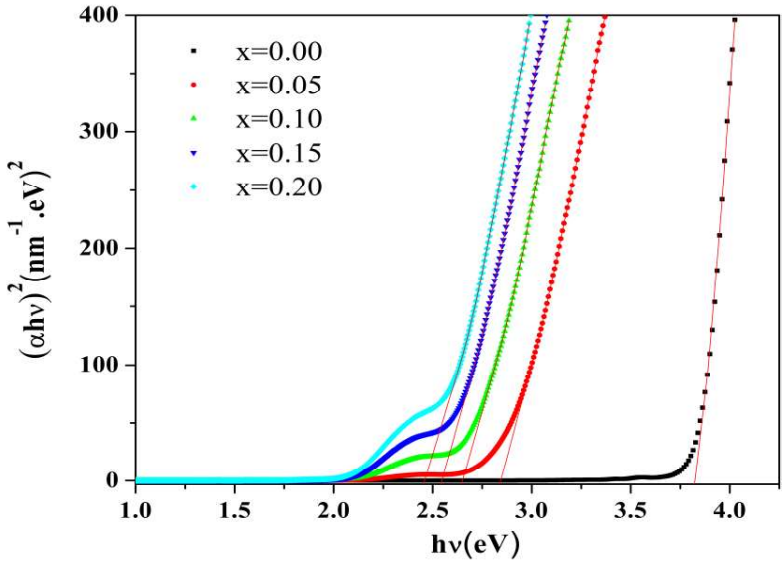

Figure 4.10 (αhν)2 versus hν with linear fits for $Dy_2Ti_{2-x}Mn_xO_7$ (x = 0, x = 0.05, x = 0.10, x = 0.15 and x = 0.20).

A decrease in the hybridization reduces the splitting between the orbitals contributing to conduction (Mn^{4+}) and valence band (O^{2-}). Additionally, the distortion of the Ti/Mn-O angle also affects the hybridization between these orbitals. Ti/Mn-O-Ti/Mn bond angle increases to 85.73° (x=0.2) from 85.21° (x = 0), which also supports the above explained inference. Hence, the different electronic configuration of Mn in comparison to Ti leads to a distortion of the local crystal field around the Mn ion. This distortion affects the orientation and energy levels of the Mn-3d orbitals, which affects the hybridization between the Mn-3d and O-2p orbitals [140], [141]. Hence, the Mn state at 455 nm shifts towards the higher wavelength side with an increase in x, and it explains the systematic variation in E_g. This establishes the optical band gap tenability through Mn inclusion at the Ti site in $Dy_2Ti_{2-x}Mn_xO_7$. Mn^{4+} absorption states are usually characterized as CTT from O^{2-} to Mn^{4+}, as well as internal $^4A_{2g}$ to $^4T_{2g}$ and $^4A_{2g}$ to $^4T_{1g}$ (3d-3d; broad band) transitions within 3d states [116].

Table 4.2 Experimental and theoretical band gap for $Dy_2Ti_{2-x}Mn_xO_7$ (x=0, x = 0.05, x = 0.10, x = 0.15 and x = 0.20).

$Dy_2Ti_{2-x}Mn_xO_7$	Eg (eV) (experimental)	Eg(eV)(theoretical)	
		LDA	LDA-1/2
x=0	3.82	2.85	4.16
x=0.05	2.84	1.60	2.05
x=0.10	2.64	1.45	1.95
x=0.15	2.54	1.43	1.92
x=0.20	2.45	1.42	1.90

4.2.2 Photoluminescence spectroscopy

Further, photoluminescence (PL) emission spectra were obtained using an excitation wavelength of 280 nm. $Dy_2Ti_2O_7$ exhibits emission peaks at 338, 360, 372, 397, 411, 419, 434, 451, 468, 483 and 493 nm. With Mn inclusion, lower wavelength emission peaks are suppressed, while the higher wavelength peaks from 451 nm onwards corresponding to CTT within Dy states remain unaffected, as shown in **Figure 4.11**.

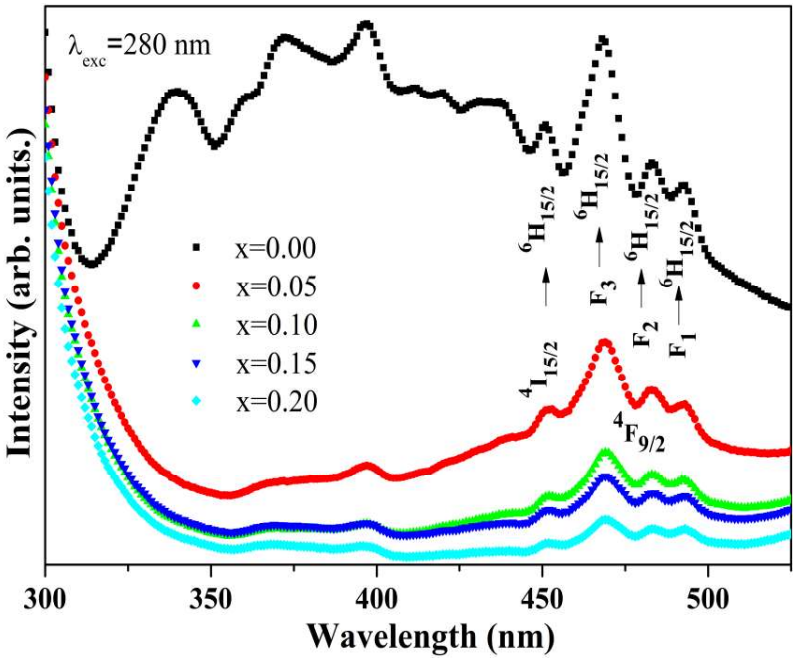

Figure 4.11 Dependence of room temperature photoluminescence (PL) emission spectra of $Dy_2Ti_{2-x}Mn_xO_7$ using an excitation wavelength of 280 nm.

Lower wavelength emission peaks of Dy^{3+} at 338, 360, 372, and 397 nm are suppressed because of the emergence of a new Mn^{3+} state due to the Jahn-Teller (JT) effect. It is basically because of the change in Mn^{4+} to Mn^{3+} state, as explained in a later section by x-ray

photoelectron spectroscopy (XPS). Evidence of the Mn^{3+} state is also observed through the dominance of the mid-band at the fermi level in the band structure of the $Dy_2Ti_{2-x}Mn_xO_7$ system using theoretical calculations the same will be discussed in a later section. CTT between the Dy^{3+} state to Mn state and between the Mn-Mn state (mixed state of Mn) results in a non-radiative transition since the energy difference between Mn^{+3} and Mn^{+4} state is too small. Hence, the JT effect is responsible for suppressing various low wavelength emission states of $Dy_2Ti_{2-x}Mn_xO_7$ with Mn inclusion. This explains the PL spectroscopy for the $Dy_2Ti_{2-x}Mn_xO_7$ system [142]. The electrons from both the Ti (300 nm) and Mn (455 nm) excited state relaxes to the excited state of Dy^{3+} through energy transfer and then relaxes to the ground state through emission. The emission peak at 451 nm corresponds to the transition from the $^4I_{15/2}$ excited state to the $^6H_{15/2}$ ground state of the Dy^{3+} ion. The other three emission peaks towards the higher wavelength side, namely 468, 483 and 493 nm, are identified as the transition from the F_3, F_2 and F_1 vibrational levels of the $^4F_{9/2}$ electronic state to $^6H_{15/2}$ electronic ground state, respectively. The emission intensity varies with the change in the extent of hybridization between Mn and its ligand atom. Weak hybridization results in an emission peak at higher energy (shorter wavelength), an increase in the hybridization shifts the emission peak towards the longer wavelength side.

Using an excitation wavelength of 455 nm, the luminescence spectra involve internal CTT within Dy-4f states at 517 nm ($^4F_{9/2}\rightarrow{}^6H_{15/2}$), 686 nm ($^4F_{9/2}\rightarrow{}^6H_{13/2}$), 734 nm ($^4F_{9/2}\rightarrow{}^6H_{11/2}$), 782 nm ($^4F_{9/2}\rightarrow{}^6H_{9/2}$) and 829 nm ($^4F_{9/2}\rightarrow{}^6H_{7/2}$) through a cross-relaxation phenomenon since the spectra do not exhibit any modification with Mn inclusion as shown in **Figure 4.12**

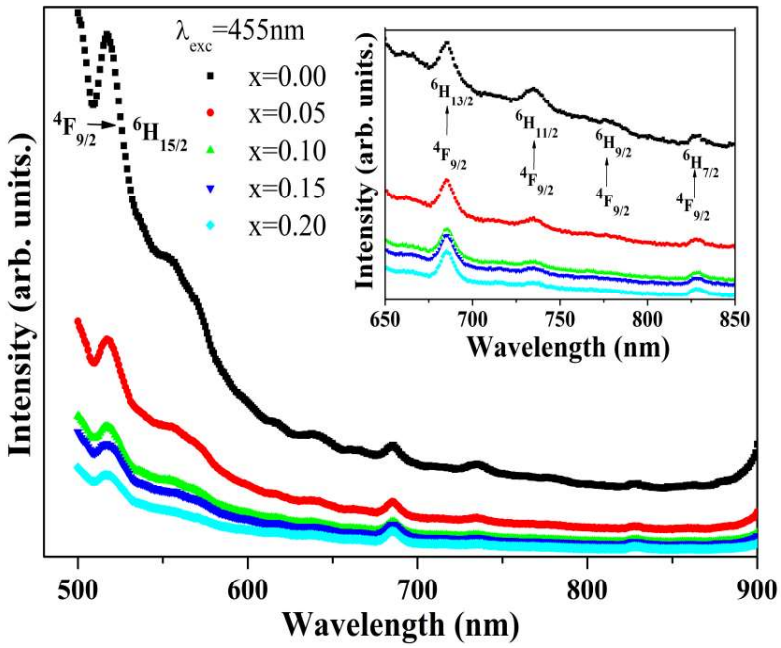

Figure 4.12 Dependence of room temperature photoluminescence (PL) emission spectra of $Dy_2Ti_{2-x}Mn_xO_7$ using an excitation wavelength of 455 nm.

The photoluminescence excitation spectrum of $Dy_2Ti_{2-x}Mn_xO_7$ (x = 0, 0.05, 0.10, 0.15, 0.20) recorded at 600 nm exhibits numerous peaks corresponding to different excitation energies as depicted in **Figure 4.13**. Analysis was performed to probe the excitation mechanism which controls the emission in this system. The spectrum indicates that the excitation of $Dy_2Ti_{2-x}Mn_xO_7$ occurs mainly through transitions from the ground state to the excited states within the 4f electron states of Dy^{3+} ions as well as due to charge transfer transition (CTT) from the valence band to the conduction band of the compound. The peak at 338 nm corresponds to the CTT excitation to the Ti-3d state of the conduction band from the O-2p state of the valence band. The peak at around 397 nm was attributed to the excitation of the $^6H_{15/2} \rightarrow {}^6P_{7/2}$ transition of Dy^{3+} ions. These lower wavelength emission peaks of Dy^{3+}at 338, 372, and 397 nm are suppressed in the $Dy_2Ti_{2-x}Mn_xO_7$ system because of the emergence of a

new Mn^{3+} state due to the Jahn-Teller (JT) effect. It may be primarily due to the change in Mn^{4+} to Mn^{3+} state, as explained in a later section by x-ray photoelectron spectroscopy (XPS). The appearance of the mid-band of the Mn state, as observed from theoretical calculations, validates this suppression as CTT processes between the Mn and O ions become prominent after Mn inclusion in the system [138].

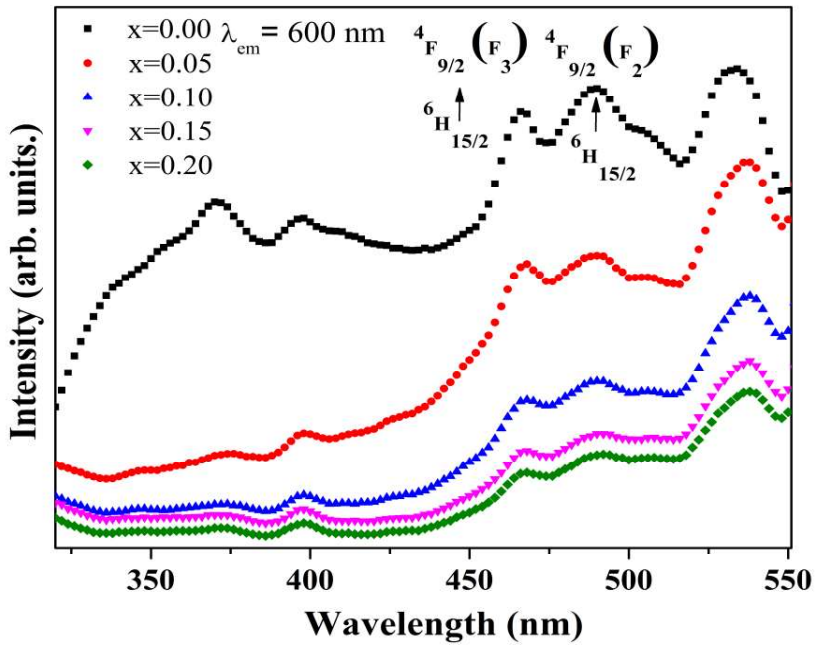

Figure 4.13 Room temperature photoluminescence (PL) excitation spectra of $Dy_2Ti_{2-x}Mn_xO_7$ using an emission wavelength of 600 nm.

As discussed above, the possible mechanism and the energy level diagram involving the absorption and emission from the Dy^{3+}, Mn^{4+}, Ti^{4+} and O^{2-} states are schematically shown in **Figure 4.14**.

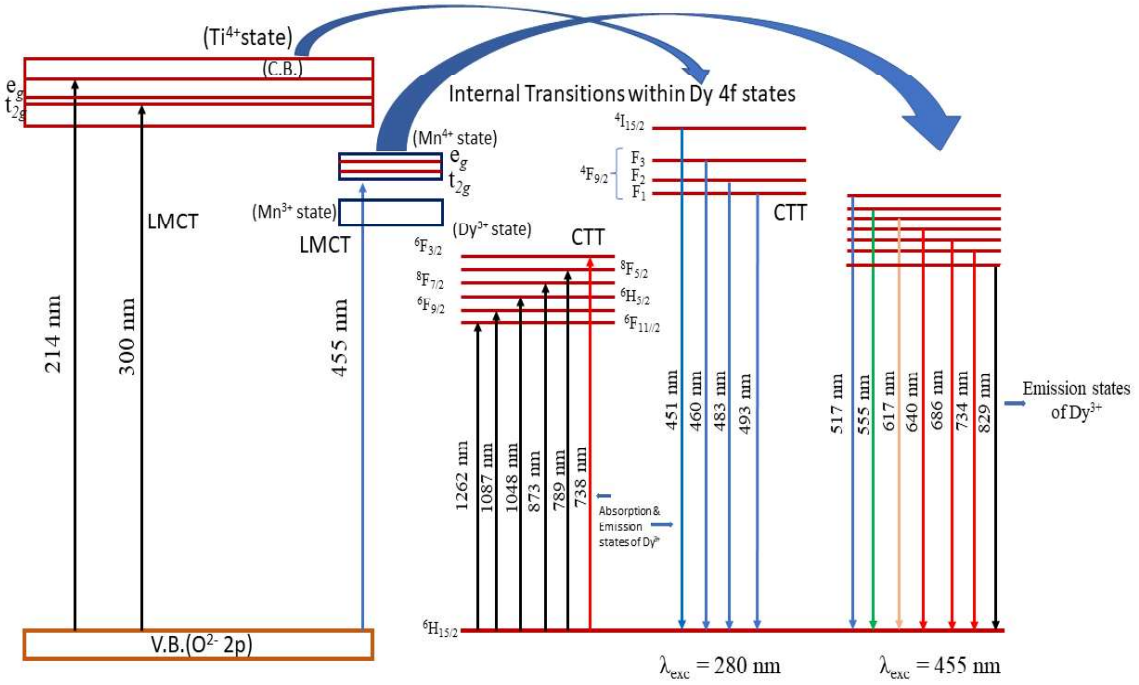

Figure 4.14 Mechanism and the energy level diagram involving the absorption and emission from the Dy^{3+}, Mn^{4+}, Ti^{4+} and O^{2-} states in $Dy_2Ti_{2-x}Mn_xO_7$

4.3 Conclusions

Electronic structure calculation and Optical study of Mn substituted pyrochlore, $Dy_2Ti_2O_7$, are presented in this manuscript. The theoretical results show that the band gap reduces with an increase in Mn concentration. Raman spectra suggest a complex interplay between the Jahn-Teller effect distortion of the octahedral structure due to the incorporation of Mn in the lattice. x-ray photoelectron spectroscopy (XPS) result indicates the presence of a mixed state of Mn, which is explained using Jahn-Teller distortion. The presence of a mixed state results in an intermediate (mid-band) Mn state between the valence band and conduction band with immediate inclusion of Mn at the Ti site in the $Dy_2Ti_{2-x}Mn_xO_7$ system. With immediate Mn inclusion at the Ti site, the absorption peak of Ti^{4+} at 300 nm shifts to 340 nm due to increase

in the angular separation with the increase in percentage inclusion of $Mn^{4+,}$ which reduces the extent of hybridization between the O-2p and Ti-3d state, resulting in the lowering of the Ti-3d energy state. Jahn-Teller effect is responsible for the presence of a mixed state of Mn (explained using x-ray photoelectron spectroscopy results), resulting in the intermediate Mn state between the valence band and conduction band with immediate inclusion of Mn at the Ti site in $Dy_2Ti_{2-x}Mn_xO_7$ system as is evident from band structure calculation. An increase in the percentage inclusion of Mn results in a sequential reduction in band-gap from 3.82 to 2.45 eV, which establishes the optical band gap tunability through Mn inclusion at the Ti site in $Dy_2Ti_{2-x}Mn_xO_7$. Such a system can be used for spin-ice based magneto-optical applications. In the next chapter, we will switch to the next class of spin frustrated system, namely XY type pyrochlore system, i.e., $Er_2Ti_2O_7$. Its magnetic and electronic studies will be discussed in the subsequent chapters.